Communications Physics

https://doi.org/10.1038/s42005-026-02591-x

Article in Press

Unusual diffusion of chiral active Brownian particles in deformable and displaceable media

Received: 18 September 2025

Accepted: 9 March 2026

Cite this article as: Zhang, K., Tian, Y., Yu, X. *et al.* Unusual diffusion of chiral active Brownian particles in deformable and displaceable media. *Commun Phys* (2026). https://doi.org/10.1038/s42005-026-02591-x

Kexin Zhang, Yuxin Tian, Xiaoting Yu, Hongwei Zhu, Yanwei Li, Mingcheng Yang, Peng Liu, Ning Zheng & Luhui Ning

Unusual Diffusion of Chiral Active Brownian Particles in Deformable and Displaceable Media

Kexin Zhang,[1] Yuxin Tian,[1] Xiaoting Yu,[1] Hongwei Zhu,[2] Yanwei Li,[1]
Mingcheng Yang,[3,4,*] Peng Liu,[1,†] Ning Zheng,[1,‡] and Luhui Ning[5,6,§]

[1] *School of Physics, Beijing Institute of Technology, Beijing 100081, China*
[2] *School of Physical Science and Technology, Key Laboratory of Magnetism and Magnetic Materials for Higher Education in Inner Mongolia Autonomous Region, Baotou Teachers' College, Baotou 014030, China*
[3] *Beijing National Laboratory for Condensed Matter Physics and Laboratory of Soft Matter Physics, Institute of Physics, Chinese Academy of Sciences, Beijing 100190, China*
[4] *School of Physical Sciences, University of Chinese Academy of Sciences, Beijing 100049, China*
[5] *Beijing Key Laboratory of Optical Detection Technology for Oil and Gas, China University of Petroleum-Beijing, Beijing 102249, China*
[6] *Basic Research Center for Energy Interdisciplinary, College of Science, China University of Petroleum-Beijing, Beijing 102249, China*

Chiral active Brownian particles convert stored or environmental energy into self-propulsion and rotation, driving systems far from equilibrium. How chirality influences diffusion in crowded environments composed of deformable and displaceable obstacles remains poorly understood. Here we show, through combined experiments and theory, that chiral active Brownian particles confined in an annular channel with deformable and displaceable ring obstacles exhibit a pronounced nonmonotonic dependence of diffusivity on obstacle density. The diffusion coefficient initially increases and then decreases with obstacle area fraction, reaching enhancements of nearly two orders of magnitude. Experiments and theory indicate that this behavior originates from a competition between obstacle-induced motion collimation and suppression of migration velocity. The enhancement also varies nonmonotonically with particle orbital radius due to differences in intrinsic free-space diffusivity. These findings provide insight into nonequilibrium transport in dynamically reconfigurable environments and suggest strategies for controlling chiral active matter in complex media.

INTRODUCTION

Chiral active particles represent a unique class of active matter capable of converting internal or environmental energy into autonomous rotation [1–4], thereby driving systems far from equilibrium and resulting in rich unconventional phenomena, including odd viscosity [5–8], odd elasticity [9–11], hyperuniformity [12, 13], anomalous transport [3, 4, 14], as well as the spontaneous emergence of rotating droplets [15–18] and microswarms [18]. Chiral active particles are observed across a wide range of systems and length scales, from nanoscale motor proteins [19], microscale sperm cells [20, 21] and interface-circling bacteria [22, 23], to chiral colloids [24, 25], starfish embryos [10], centimeter-scale vibrated robots and rotors [26–34], and chiral active polymers [35]. In particular, chiral active Brownian particles (CABPs) combine self-propulsion with autonomous rotation, proving a ubiquitous and powerful model for probing the fundamental principles of nonequilibrium statistical mechanics and active matter physics.

In free space, CABPs typically follow circular trajectories in two dimensions and helical paths in three dimensions [1], while their chirality further modulates orientational persistence and can generate oscillatory kurtosis under strong torque conditions [36]. However, in biologically relevant environments such as soil [37], hydrogels [38, 39], and living tissues [40, 41], particles often encounter disordered, confined and often dynamically evolving microstructures. In such contexts, CABPs transport can deviate significantly from that in homogeneous systems [42–45], exhibiting phenomena such as directional locking [3], spin-dependent segregation [46, 47], chirality-induced steady momentum currents and bulk accumulation [48], deviations from Maxwell-Boltzmann behavior that vanish when chirality or radial symmetry is absent [49], and chirality-density coupling that renormalizes orientational persistence and generates nontrivial dynamical crossovers [50]. CABPs exhibit pronounced diffusion enhancement in disordered obstacles [4, 51–53], a similar counterintuitive enhancement has recently been observed for self-propelled polymer-like worms in disordered media [54], in stark contrast to the diffusion suppression typically observed for linear self-propelled particles under analogous conditions [55–58]. Numerical simulations by van Roon *et al.* further indicate that the diffusivity of CABPs depends nonmonotonically on obstacle density, arising from the interplay between chirality and static disorder that induces orbit rectification and channeling [4]. This characteristic nonmonotonic response, rooted in the redirection of intrinsic self-propulsion, represents a transport mechanism specific to CABPs and is

* mcyang@iphy.ac.cn
† liupeng@bit.edu.cn
‡ ningzheng@bit.edu.cn
§ lhningphy@cup.edu.cn

absent in pure rotors lacking self-propulsion [59]. Collectively, these results underscore the role of chirality in particle-environment interactions and indicate that obstacle disorder, noise, and density act as tunable parameters for active transport.

Despite these advances, previous studies have primarily focused on rigid and immobile obstacles. In contrast, obstacles in biologically relevant settings, such as cell aggregates and extracellular matrices, are deformable, displaceable, and often capable of structural reorganization. The diffusion dynamics of CABPs in such environments remain poorly understood, limiting our ability to predict and control diffusive behaviors in biologically relevant contexts.

In this paper, we combine experiments with theory to investigate the diffusion dynamics of CABPs confined within annular channels embedded with deformable, displaceable, and ring-shaped obstacles. Both experimental measurements and theoretical analyses reveal a nonmonotonic dependence of the diffusion coefficient on the obstacle area fraction, which arises from two competitive effects between the obstacle-induced enhancement of CABPs motion collimation and reduction in their migration velocity. Furthermore, the maximum diffusion enhancement also exhibits a nonmonotonic relationship with the orbital radius of CABPs, due to the intrinsic differences in their free-space diffusive capability at different orbital radii.

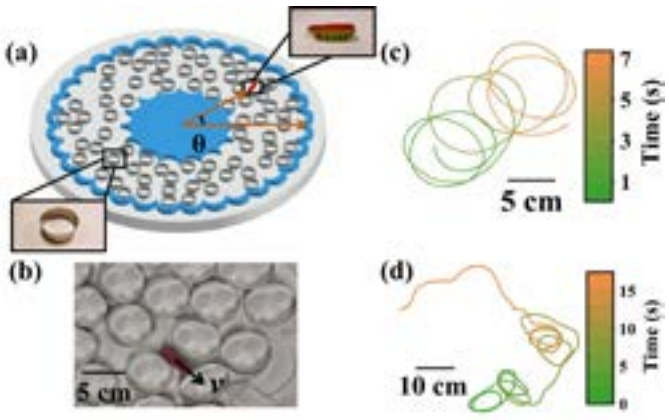

FIG. 1. Experimental setup and trajectories of chiral active Brownian particles. (a) Experimental setup at an obstacle area fraction of $\phi = 0.30$. A red marker is affixed to the back of the robot, gray circles denote soft-ring obstacles, and blue regions indicate system boundaries. θ represents the polar angle of the CABP relative to the x-axis. (b) Deformation of soft rings under compressive stress exerted by CABP motion. Black arrow indicates the direction of motion. Time-colored trajectory of a CABP with $r = 4.46$ cm in the (c) absence of obstacles and (d) presence of obstacles at $\phi = 0.50$, with the color bar representing the time from the beginning (green) to the end (orange).

Robot	**1**	**2**	**3**	**4**	**5**
r (cm)	2.85	3.76	3.88	4.46	6.41
v_0 (cm · s^{-1})	24.04 ± 0.94	23.39 ± 1.11	22.28 ± 0.70	26.12 ± 0.61	24.95 ± 0.75
ω_0 (s^{-1})	8.43 ± 0.24	6.23 ± 0.21	5.73 ± 0.13	5.85 ± 0.21	3.89 ± 0.28
T (s)	0.74	1.01	1.10	1.07	1.61
D_r (s^{-1})	0.39 ± 0.095	0.24 ± 0.053	0.14 ± 0.023	0.24 ± 0.064	0.27 ± 0.071
τ_r (s)	2.56	4.17	7.14	4.17	3.70
l (cm)	61.44 ± 2.4	97.54 ± 4.6	40.91 ± 5.0	108.9 ± 2.5	92.32 ± 2.8

TABLE 1. Parameters of Hexbugs used in the experiments. r, v_0, ω_0, T, D_r, τ_r, and l represent the orbital radius, the translational velocity, angular velocity, the cycle period, the rotational diffusion coefficient, the persistence time, and the persistence length in the absence of obstacles.

RESULTS

In our experiment, CABPs were modeled using Hexbug robots, each powered by an internal miniature motor that drives planar self-propulsion through twelve slightly backward-bent elastic legs [top of Fig. 1(a)]. By tuning the asymmetry between the two rows of legs, five distinct Hexbug robots with varying orbital radii r were obtained, with their respective parameters listed in Table. 1. θ is defined as the angle between the robot's position vector and the x-axis. The representative trajectories of a CABP with $r = 4.46$ cm in the absence [Fig. 1(c)] and presence of obstacles at blue $\phi = 0.50$ [Fig. 1(d)]. The ring-shaped obstacles, composed of thin stainless-steel ribbons, are flexible and readily deform or displace upon contact with robots [Fig. 1(b)], thereby forming a dynamically reconfigurable medium.

We first investigate the diffusion of CABPs in annular channels with various area fractions of soft-ring obstacles, $\phi = N_r S_r / S$, where N_r is the number of rings, S_r is the area of a single ring, and S is the total channel area. The dynamics of CABPs are quantified by the mean square displacement (MSD) of the angular coordinate θ, evaluated in a polar coordinate system centered at the disk origin for different time interval t [Fig. 2(a)]. At short time, the MSD exhibits a ballistic scaling, MSD $\propto t^2$, reflecting the circular motion. After many orbital cycles, it crosses over to a normal diffusion regime with MSD $\propto t$ at long times [3], from which the long-time diffusion coefficient D is extracted via MSD $= \langle [\theta(t_0 + t) - \theta(t_0)]^2 \rangle = 2Dt$. Figure 2(b) plots the normalized diffusion coefficient D/D_0 as a function of ϕ for CABPs with different orbital radii r, where D_0 is the obstacle-free diffusion coefficient shown in Fig. 2(c). D/D_0 exhibits a pronounced nonmonotonic dependence on ϕ. As ϕ increases, diffusion significantly enhances and reaches a peak within the range of $\phi = 0.6 - 0.75$. This enhancement is especially prominent for CABPs with smaller r, where D/D_0 approaches 60, nearly two orders of magnitude greater than without obstacles. At higher ϕ, motility is reduced due to crowding, resulting in a gradual decline of D/D_0. When $\phi \geq 0.8$,

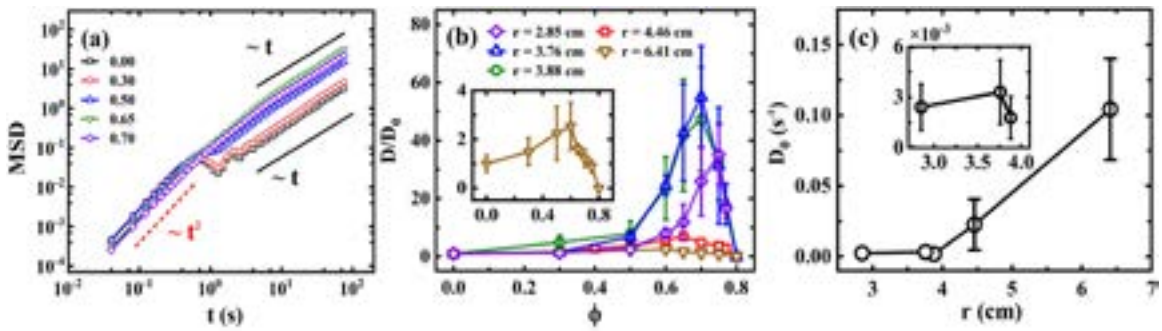

FIG. 2. Diffusion dynamics of chiral active Brownian particles. (a) MSD of a CABP with $r = 4.46$ cm as a function of delay time t at different ϕ. Solid black lines indicate linear scaling, MSD $\sim t$, characteristic of the normal diffusion. (b) The relation between ϕ and D/D_0 for CABPs with $r = 2.85$, 3.76, 3.88, 4.46 and 6.41 cm. Inset: D/D_0 of CABP with $r = 6.41$ cm. (c) Diffusion coefficient D_0 for five CABPs in the absence of obstacles. Inset: D_0 for CABPs with $r = 2.85$, 3.76, and 3.88 cm. Error bars denote the standard deviation from 3–7 independent measurements and are not visible when smaller than the symbol size.

all CABPs are effectively trapped near their initial positions, *i.e.*, D/D_0 approaches zero. Additional control experiments varying obstacle size, softness, and confinement geometry consistently confirm the robustness of this nonmonotonic diffusion behavior of CABPs [Supplementary Note 1-3]. whereas no such nonmonotonic behavior is observed for achiral particle [Supplementary Note 4].

Two dynamical states of CABPs in obstacles

To elucidate the nonmonotonic dependence of D/D_0 of CABPs on obstacle area fraction ϕ, we identify two representative dynamical states that emerge in the presence of flexible obstacles, referred to as the trapped state and the migrating state. In the trapped state, CABPs interact with surrounding soft rings through collisions, displacing them to form transient, obstacle-depleted regions. Within these regions, CABPs exhibit confined circular motion, resulting in markedly suppressed diffusion, as exemplified by a CABP with an orbital radius of 3.88 cm at an obstacle area fraction of 0.60 [Supplementary Movie 1]. The CABP is defined as being in the trapped state if it remains within a circular region of radius R_c centered at its initial position and completes at least two rotations. The confinement radius R_c is determined by the characteristic confinement scale at a given obstacle area fraction ϕ and is defined as the average diameter of all identified trapped regions [Supplementary Note 5]. Otherwise, if the residence time within the R_c region is shorter than two rotational periods, the CABP is classified as being in the migration state. Increasing this threshold to three rotations yields nearly identical trapping durations, confirming the robustness of this definition [Supplementary Note 6]. In the migrating state, CABPs undergo successive inelastic collisions with surrounding deformable rings, which gradually reorient their motion and support sustained quasi-linear trajectories, as illustrated by a particle with an orbital radius of 3.88 cm at $\phi = 0.70$ [Supplementary Movie 2]. The non-circular shapes observed in the videos mainly arise from experimental and imaging factors rather than irreversible deformation. In particular, local curvature variations result from the tape used to fix the soft rings, while the imaging geometry introduces slight distortions near the ring boundaries. The small elastic deformations of the rings were quantified at different obstacle area fractions ϕ in the presence of a CABP with $r = 3.76$ cm [Supplementary Note 7]. We speculate that substantially stronger deformations, such as leading to rod-like or highly elongated obstacles, may potentially modify the transport behavior and warrant future investigation.

To further investigate the two distinct dynamical states of CABPs in flexible and crowded environments, we analyze the self-part of the two-point overlap correlation function $Q(t)$ [60], defined as

$$Q(t) = \left\langle \frac{1}{N} \sum_{i=1}^{N} q(|\theta(t_i + t) - \theta(t_i)|) \right\rangle, \tag{1}$$

where $\langle\ \rangle$ denotes ensemble averaging, N is the number of temporal averages, and $\theta(t)$ is the polar angle of the CABP at a time interval t. The characteristic function $q(|\Delta\theta|)$ is given by

$$q(|\Delta\theta|) = \begin{cases} 1, & \text{if } |\Delta\theta| < b, \\ 0, & \text{otherwise,} \end{cases} \tag{2}$$

which quantifies the probability that a CABP remains within an angular window of width $2b$ over a time interval t. Here, the angular threshold parameter is defined as $b = 3\arcsin[r/(R_{in} + r)]$, where $R_{in} = 20.0$ cm represents the maximum radial distance from the system center to the inner boundary. Detailed procedures for determining b are provided in the Supplementary Note 8. A comprehensive sensitivity analysis confirms that

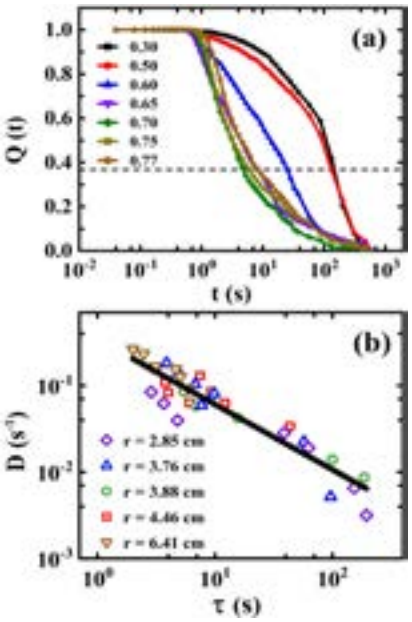

FIG. 3. Relaxation dynamics and scaling behavior. (a) Self-overlap function $Q(t)$ for a CABP with $r = 3.76$ cm at different ϕ. (b) Scaling relation between the diffusion coefficient D and the relaxation time τ for different CABPs at various ϕ. The solid black line represents a power-law fit of $D \propto \tau^{-0.75}$.

the results are robust across a broad parameter range $b \in (0.38, 0.98)$ for the five different CABPs. This universality does not diminish the fundamental role of chirality. Instead, the coexistence of trapped and migratory states, which underlies the observed dynamical heterogeneity, arises directly from particle chirality. The chirality-driven circular motion couples with deformable obstacles and induces intermittent transitions between these two states.

The temporal decay of $Q(t)$ characterizes the system's relaxation dynamics, and the relaxation time τ is defined as the time when $Q(t)$ decays to 1/e [Fig. 3(a)]. Relaxation is dominated by slow modes, whereas diffusion predominantly reflects faster processes. The scaling relation between the diffusion coefficient D and the relaxation time τ, $D \propto \tau^{-\kappa}$, provides as a sensitive indicator of dynamic heterogeneity. $\kappa = 1$ indicates a dynamically homogeneous systems, while $\kappa < 1$ signifies the presence of heterogeneous dynamics [60, 61]. As shown in Fig. 3(b), the diffusion coefficient and relaxation time for CABPs with various r exhibit a power-law relation $D \propto \tau^{-0.75}$, indicative of significant dynamical heterogeneity in the motion of CABPs within obstacle-rich environments. This heterogeneity arises from the coexistence of two dominant motility modes, namely a slow, localized trapped state and a fast, persistent migration state, as exemplified by CABP motion in the presence of obstacles at $\phi = 0.50$ [Fig. 1(d)]. The data for CABPs with different r collapse onto a unified scaling curve, implying that the observed dynamical heterogeneity is largely independent of chirality and exhibits universal features.

Nonmonotonic dependence of D/D_0 on obstacle area fraction

The effective diffusion of CABPs is thus governed by the competition of these two states. Migrating motion facilitates longrange displacement, while intermittent trapping reduces effective transport, collectively leading to a nonmonotonic variation of the normalized diffusion coefficient D/D_0 with ϕ. Figures 4(a)-(e) present the normalized migration time t_m/t_{tot} and normalized velocity v/v_0 for various CABPs as functions of the obstacle area fraction ϕ. Here, the migration time t_m is defined as the cumulative duration that a CABP spends in the migration state during a single experimental run, and t_{tot} denotes the total duration of that run. The velocities v and v_0 are obtained by averaging the frame-to-frame displacement divided by the frame interval over the full trajectory in the presence and absence of obstacles, respectively. As ϕ increases, the deformable rings create channel-like pathways that promote persistent directional migration, significantly enhancing the nonlocal diffusion of CABPs and leading to a progressive increase in the migration time t_m. At sufficiently high ϕ, CABPs remain predominantly in the migrating state with $t_m/t_{tot} \to 1$, and trapping events become negligible. However, sustained migration at low velocity yields limited net displacement, *i.e.*, t_m alone is inadequate to characterize the diffusion ability. A comprehensive evaluation of CABP diffusion thus necessitates accounting for both the migration time t_m and corresponding translational velocity v. As obstacle area fraction increases, sustained obstruction by soft rings gradually reduce the migration speed v, which eventually approaches zero due to overcrowding-induced immobilization. At moderate densities, however, the flexible obstacles facilitate a transition from chiral orbital motion to directional migration, thereby enhancing diffusion. With further increase in ϕ, the continued suppresses of v becomes dominant, reducing particle mobility. The competition between enhanced collimation of CABP motion and suppressed migration velocity gives rise to a critical area fraction ϕ_c, at which the diffusive coefficient D attains its maximum, leading to the observed nonmonotonic dependence of D/D_0 on ϕ.

To validate the competing mechanisms underlying CABP diffusion, we evaluate the ratio $v^2 t_m/(v_0^2 t_{tot})$, which captures the combined effects of obstacle-induced motion collimation and velocity suppression. As the obstacle area fraction increases, CABP-obstacle collisions reduce the migration speed v while simultaneously enhancing directional persistence, as reflected by an increase in t_m. Because the product $v^2 t_m$ has the same physical dimension as the diffusion coefficient, the normalized ratio provides a natural, dimensionless measure of the effective diffusion behavior. As shown in Fig. 5(a), $v^2 t_m/v_0^2 t_{tot}$ exhibits a pronounced nonmonotonic dependence on ϕ, closely following the trends observed in the experimental diffusion coefficient D/D_0 [Fig. 2(b)]. Furthermore, the critical obstacle area fraction ϕ_c, obtained

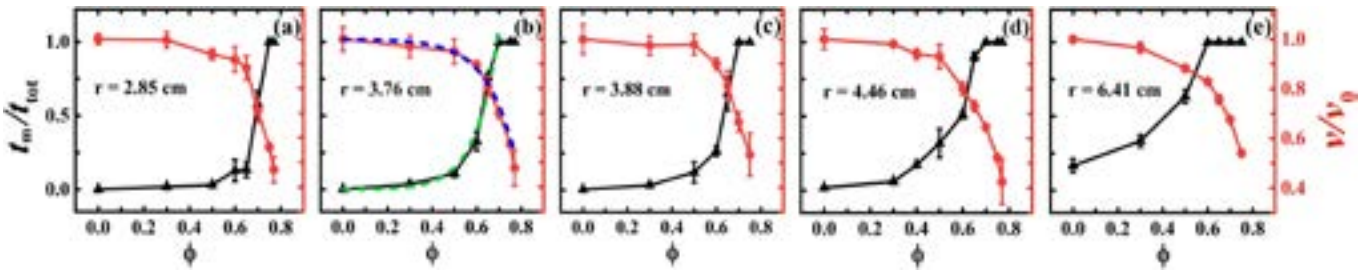

FIG. 4. The migration time and velocity. Normalized migration time (black triangles) and normalized velocity (red circles) of CABPs with (a) $r = 2.85$ cm, (b) $r = 3.76$ cm, (c) $r = 3.88$ cm, (d) $r = 4.46$ cm, and (e) $r = 6.41$ cm, as functions of ϕ. Green and blue dashed lines in (b) represent fits to the data using empirical functions $t_m/t_{tot} = A_1 e^{b_1\phi}$ and $v/v_0 = 1/(y_2 + A_2 e^{b_2\phi})$, respectively. Error bars represent the standard deviation from 3–7 independent measurements and are not visible when smaller than the symbol size.

from the experimental diffusion coefficient D/D_0 and the empirical prediction, yields consistent values and systematically shifts toward smaller ϕ with increasing orbital radius r [Fig. 5(c)]. These results confirm that the observed nonmonotonic diffusion enhancement arises from the competition between the obstacle-induced enhancement of CABP motion collimation and the suppression of their migration velocity.

In the annular channel geometry, CABP motion along the azimuthal direction θ is effectively unconfined and experiences periodic boundary conditions, allowing the angular displacement $\Delta\theta$ can exceed 2π. Across the explored obstacle area fraction ϕ, the mean radial coordinate remains approximately constant [Supplementary Note 9], indicating that radial fluctuations have a negligible influence on longtime transport. Diffusion can therefore be characterized by the angular diffusion coefficient, which can be converted to the corresponding translational diffusivity through the mean radial coordinate. Under obstacle-free conditions, the effective diffusion coefficient of a CABP can be expressed theoretically as [36, 62, 63],

$$D_0 = D_t^T + \frac{v_0^2 \tau_r}{2\left[1 + (\omega_0 \tau_r)^2\right]}. \tag{3}$$

Since the thermal contribution D_t^T is negligibly compared with the activity-induced term, the effective diffusion coefficient can be approximated as

$$D_0 \approx \frac{v_0^2 \tau_r}{2\left[1 + (\omega_0 \tau_r)^2\right]}. \tag{4}$$

Here $v_0 = F_d/\gamma_t^0$ and $\omega_0 = T_d/\gamma_r^0$, where γ_t^0 and γ_r^0 denote the translational and rotational friction coefficients in obstacle-free space, while F_d and T_d are the driving force and torque acting on the particle. The persistence time is defined as $\tau_r = 1/D_r$ [62], where D_r is obtained from the mean-squared angular displacement or the orientation autocorrelation [64, 65]. For the Hexbug systems, $D_r \propto \gamma_r^{-1}$ and can be written as $D_r = E_{eff}\gamma_r^{-1}$, where the proportionality factor E_{eff} is related to the effective thermal energy. E_{eff} can be reasonably assumed to remain unchanged with and without obstacles since the energy input originates from the Hexbug itself.

In obstacle-rich environments, increasing obstacle area fraction ϕ modifies both translational and rotational dynamics. Frequent collisions reduce the migration speed, effectively increasing the translational friction $\gamma_t(\phi)$, while obstacle-induced alignment enhances orientational persistence, thereby reducing the rotational diffusion coefficient and increasing the effective rotational friction $\gamma_r(\phi)$. Both friction coefficients are therefore treated as ϕ-dependent. Experimentally, they are captured by the empirical relations $\gamma_r(\phi) \propto t_m/t_{tot}$ and $\gamma_t(\phi) \propto v_0/v$, which quantify the enhancement of directional persistence and the suppression of migration speed, respectively. Substituting these relations into Eq. (4) yields the effective diffusion coefficient for obstacle-free and obstacle-rich environments,

$$D_0 = \frac{F_d^2 \gamma_r^0}{2E_{eff}(\gamma_t^0)^2[1 + (E_{eff}^{-1} T_d)^2]}, \tag{5}$$

$$D = \frac{F_d^2 \gamma_r(\phi)}{2E_{eff}\gamma_t^2(\phi)[1 + (E_{eff}^{-1} T_d)^2]}, \tag{6}$$

leading to the normalized diffusion coefficient

$$\frac{D}{D_0} = \frac{\gamma_r(\phi)(\gamma_t^0)^2}{\gamma_t^2(\phi)\gamma_r^0}. \tag{7}$$

As shown in Figs. 4(a)-(e), the normalized migration duration t_m/t_{tot} increases with ϕ and approaches unity at high obstacle densities, while the normalized velocity v/v_0 decreases correspondingly, indicating a confinement-induced transition from rotational to directed motion. Both dependences are well captured by the empirical functions $t_m/t_{tot} = A_1 e^{b_1\phi}$ and $v/v_0 = 1/(y_2 + A_2 e^{b_2\phi})$, from which the scaling forms of the friction coefficients are extracted as $\gamma_r(\phi) = \gamma_r^0 e^{b_1\phi}$ and $\gamma_t(\phi) \approx \gamma_t^0[1 + (A_2/y_2)e^{b_2\phi}]$.

We take a CABP with an orbital radius of $r = 3.76$ cm as a representative case. The exponential fits for t_m/t_{tot}

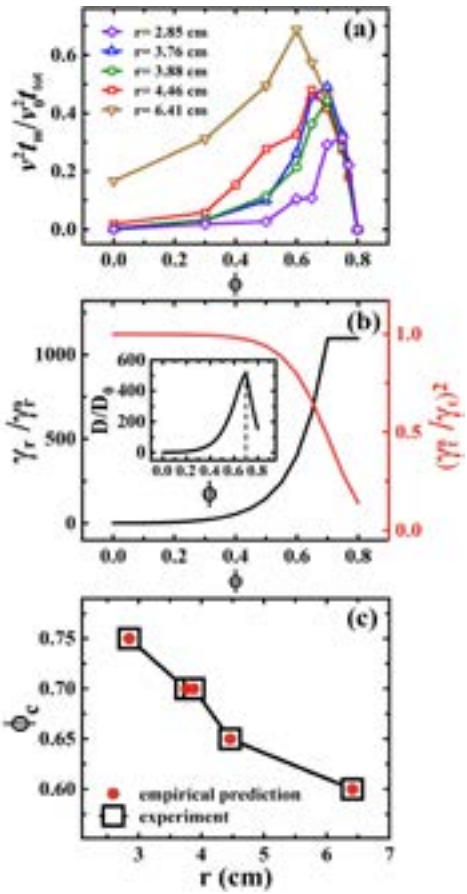

FIG. 5. Dynamics and critical behavior of chiral active Brownian particles. (a) The relations between $v^2 t_m/v_0^2 t_{tot}$ of different CABPs and ϕ. (b) The empirical predictions of the normalized rotational friction coefficient γ_r/γ_r^0 (black line) and translational friction coefficient $(\gamma_t^0/\gamma_t)^2$ (red line) of a CABP with $r = 3.76$ cm, as functions of ϕ. Inset: The empirical predicted normalized diffusion coefficient D/D_0 versus ϕ, exhibiting a peak at $\phi = 0.70$. (c) Critical area fraction ϕ_c corresponding to the peak of experimentally measured D/D_0 (black squares) and empirical prediction (red dots) for CABPs with different r.

and v/v_0, shown as green and blue dashed lines in Fig. 4(b), excellently describe the experimental data with parameters $A_1 = 0.001$, $b_1 = 10$, $y_2 = 1.0$, $A_2 = 4.5\times10^{-5}$, and $b_2 = 13$. On this basis, the empirical prediction from Eq. (7), presented in the inset of Fig. 5(b), successfully reproduces the trends observed in both the experimental diffusion coefficient D/D_0 [blue triangles in Fig. 2(b)] and $v^2 t_m/v_0^2 t_{tot}$ [blue triangles in Fig. 5(a)]. The same empirical fitting functions and scaling analysis were applied to four additional CABPs with different orbital radii r, all of which show consistent agreement with the observed trends [Supplementary Note 10]. Furthermore, the critical obstacle area fraction ϕ_c, obtained from the experimental diffusion coefficient D/D_0 and the empirical prediction, yields consistent values and systematically shifts toward smaller ϕ with increasing orbital

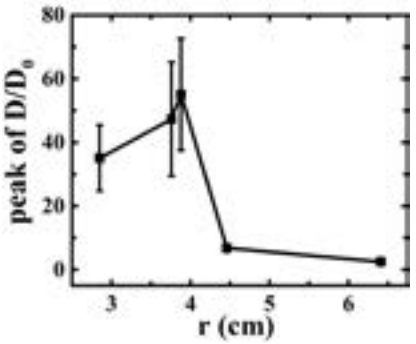

FIG. 6. The peak of the normalized diffusion coefficient. The relation between the peak of D/D_0 and r for chiral active Brownian particles. Error bars represent the standard deviation from 3–7 independent measurements.

radius r [Fig. 5(c)]. These results demonstrate that the empirical functions together with the scaling arguments capture the essential physics underlying the experimentally observed nonmonotonic diffusion of CABPs in complex media.

Nonmonotonic dependence of the diffusion peak D/D_0 on the orbital radius

Figure 2(b) demonstrates not only the nonmonotonic dependence of D/D_0 on the obstacle area fraction ϕ, but also a pronounced variation in the magnitude of enhancement among different CABPs. The peak of D/D_0 itself varies nonmonotonically with the orbital radius [Fig. 6]. CABPs with smaller orbital radii ($r = 2.85$, 3.76, and 3.88 cm) exhibit strong diffusion enhancement with $D/D_0 > 40$, while those with larger radii ($r = 4.46$ and 6.41 cm) show only modest enhancement ($D/D_0 < 10$). This disparity primarily originates from intrinsic differences in their free-space diffusive capability: the baseline diffusive coefficient D_0 increases with the orbital radius r [Fig. 2(c)], as illustrated by representative free-space trajectories of CABP with $r = 6.41$ cm [Fig. 7(a)] and 2.85 cm [Fig. 7(c)] at $\phi = 0.0$. In contrast, in the presence of soft-ring obstacles, the maximum diffusive capabilities attained by CABPs with $r = 6.41$ cm [Fig. 7(c)] and 2.85 cm [Fig. 7(d)] become comparable. Consequently, the relative diffusion enhancement is significantly larger for CABPs with smaller orbital radius ($r = 2.85$ cm), indicating that the obstacle-induced collimation disproportionately enhances the transport of CABPs with different r. Thus, soft-ring obstacles not only facilitate diffusion overall but also induce a radius-dependent modulation of transport efficiency. Additionally, the critical obstacle area fraction ϕ_c decreases monotonically with increasing r [Fig. 5(c)], a consequence of the higher collision frequency experienced by larger-radius CABPs at a given ϕ, which accelerates directional reorientation and drives a transition from orbital to directed migration. Conse-

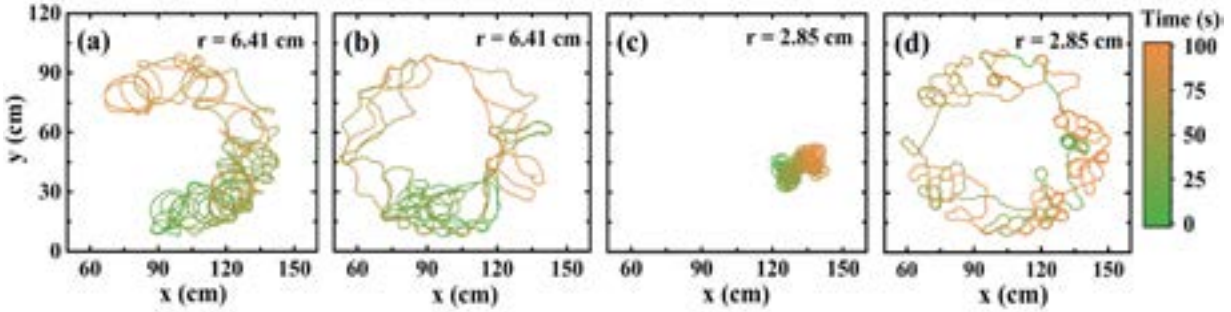

FIG. 7. Trajectories of chiral active Brownian particles. (a)-(b) Trajectories of the CABP with $r = 6.41$ cm in free space ($\phi = 0$) and an environment with soft-ring obstacle at $\phi = 0.60$, respectively. (c)-(d) Trajectories of the CABP with $r = 2.85$ cm at $\phi = 0$ and $\phi = 0.75$. All trajectories are recorded over a duration of $\Delta t = 100$ s, and the color bar represents the time from the beginning (green) to the end (orange).

quently, optimal transport and maximal diffusion occur at lower ϕ_c for larger–radius CABPs.

DISCUSSION

Using experimental measurements and theoretical modeling, we have systematically investigate the diffusion dynamics of CABPs confined within annular channels embedded with deformable and displaceable ring-shaped obstacles at varying area fraction. A pronounced nonmonotonic dependence of the normalized diffusion coefficient D/D_0 on the obstacle area fraction ϕ was identified, with strongly enhanced diffusivity at intermediate ϕ, followed by suppression at higher densities. Both experiments and theory consistently demonstrate that this nonmonotonicity originates from the interplay between two competing effects, namely the enhancement of CABP motion collimation and the suppression of their migration velocity as increasing obstruction. The enhancement in diffusivity was found to be more significant for CABPs with smaller orbital radii, where lower intrinsic diffusivity leads to stronger susceptibility to confinement-induced motion collimation. A robust scaling relation, $D \propto \tau^{-\kappa}$ with $\kappa < 1$, was further uncovered, revealing pronounced dynamical heterogeneity characterized by the coexistence of intermittent trapping and longrange migration. The results highlight the critical influence of flexible confinement in regulating active transport and reveal a radius-dependent selection mechanism by which the transport of less diffusive particles is preferentially enhanced. Beyond clarifying the competing mechanisms governing CABP dynamics in deformable and crowded environments, this work establishes a conceptual framework for understanding structure-sensitive transport and chirality-dependent behavior in both biological and synthetic active systems. These insights open avenues for future studies, including obstacle stiffness modulation and spatial heterogeneity, to achieve controlled active navigation in complex environments.

METHODS

Experimental setup

The Hexbug robots used in the experiments measured 4.3 cm in length and 1.3 cm in width. They are confined within an annular channel approximately 23.0 cm in width, effectively emulating periodic boundary conditions. To suppress persistent sliding along the channel boundaries, both the inner and outer boundaries were constructed from petal-shaped arc segments [66], with 16 and 32 segments, respectively, each subtending a central angle of 160° [Fig. 1(a)]. Flexible obstacles consisted of mobile soft rings with a diameter of $\sigma = 4.90$ cm, fabricated from 0.02 mm-thick stainless steel ribbons.

Data acquisition and CABP dynamic analysis

Each experimental run was limited to 15 minutes to ensure stable propulsion speeds, and batteries were replaced before each run to maintain consistency across trials [30]. Images of the sample were recorded with approximately 10 minutes by a camera at 25 frames·s^{-1}. For each CABP and obstacle area fraction ϕ, 3–7 independent measurements were performed under identical conditions, yielding an ensemble of long-time diffusion coefficients D. The error bars shown in Fig. 2(b) represent the statistical variability across these measurements and increase near the critical density ϕ_c, where CABPs stochastically switch between trapped and migrating states with the variable relative duration of these states. CABP trajectories were extracted using particle recognition and tracking software, aided by a red marker affixed to the back of each robot to facilitate accurate image-based tracking. For CABP moving in free space, the mean translational velocity v_0 was obtained by averaging the displacement between consecu-

tive frames divided by the frame interval over the entire trajectory. The angular velocity ω_0 was determined by tracking the particle orientation in each frame and averaging the angular increment per unit time. The orbital radius was defined as $r = v_0/\omega_0$, and the rotation period as $T = 2\pi/\omega_0$. The effective rotational diffusion coefficient D_r was extracted from the mean squared angular displacement (MSAD), $\langle[\varphi(t_0+t)-\varphi(t_0)]^2\rangle = \omega^2 t^2 + 2D_r t$ [Supplementary Note 11], where $\varphi(t)$ denotes the orientation angle of the particle's major axis [64]. The persistence time was then defined as $\tau_r = 1/D_r$ [49], and the corresponding persistence length as $l = v_0\tau_r$.

DATA AVAILABILITY

The data supporting the findings of this study are available in the main text and Supplementary information. Supplementary Movie 1 and Supplementary Movie 2 are uploaded as Supplemental Material, and the data used to obtain in the plots are available as the Supplementary Data. Additional information is available from the corresponding author upon request.

REFERENCES

[1] Liebchen, B. & Levis, D. Chiral active matter. *Europhys. Lett.* **139**, 67001 (2022).

[2] Shankar, S., Souslov, A., Bowick, M. J., Marchetti, M. C. & Vitelli, V. Topological active matter. *Nat. Rev. Phys.* **4**, 380–398 (2022).

[3] Chan, C. W. *et al.* Chiral active particles are sensitive reporters to environmental geometry. *Nat. Commun.* **15**, 1406 (2024).

[4] Van Roon, D. M., Volpe, G., da Gama, M. M. T. & Araújo, N. A. The role of disorder in the motion of chiral active particles in the presence of obstacles. *Soft Matter* **18**, 6899–6906 (2022).

[5] Banerjee, D., Souslov, A., Abanov, A. G. & Vitelli, V. Odd viscosity in chiral active fluids. *Nat. Commun.* **8**, 1573 (2017).

[6] Lou, X. *et al.* Odd viscosity-induced hall-like transport of an active chiral fluid. *Proc. Natl. Acad. Sci. U.S.A.* **119**, e2201279119 (2022).

[7] Mecke, J., Gao, Y., Ramírez Medina, C. A., Gompper, G. & Ripoll, M. Simultaneous emergence of active turbulence and odd viscosity in a colloidal chiral active system. *Commun. Phys.* **6**, 324 (2023).

[8] Soni, V. *et al.* The odd free surface flows of a colloidal chiral fluid. *Nat. Phys.* **15**, 1188–1194 (2019).

[9] Kole, S. J., Alexander, G. P., Ramaswamy, S. & Maitra, A. Layered chiral active matter: Beyond odd elasticity. *Phys. Rev. Lett.* **126**, 248001 (2021).

[10] Tan, T. H. *et al.* Odd dynamics of living chiral crystals. *Nature (London)* **607**, 287–293 (2022).

[11] Scheibner, C. *et al.* Odd elasticity. *Nat. Phys.* **16**, 475–480 (2020).

[12] Huang, M., Hu, W., Yang, S., Liu, Q. & Zhang, H. Circular swimming motility and disordered hyperuniform state in an algae system. *Proc. Natl. Acad. Sci. U.S.A.* **118**, e2100493118 (2021).

[13] Zhang, B. & Snezhko, A. Hyperuniform active chiral fluids with tunable internal structure. *Phys. Rev. Lett.* **128**, 218002 (2022).

[14] Chopra, P., Quint, D., Gopinathan, A. & Liu, B. Geometric effects induce anomalous size-dependent active transport in structured environments. *Phys. Rev. Fluids* **7**, L071101 (2022).

[15] Riedel, I., Kruse, K. & Howard, J. A self-organized vortex array of hydrodynamically entrained sperm cells. *Science* **309**, 300–303 (2005).

[16] Patra, P. *et al.* Collective migration reveals mechanical flexibility of malaria parasites. *Nat. Phys.* **18**, 586–594 (2022).

[17] Denk, J., Huber, L., Reithmann, E. & Frey, E. Active curved polymers form vortex patterns on membranes. *Phys. Rev. Lett.* **116**, 178301 (2016).

[18] Liebchen, B. & Levis, D. Collective behavior of chiral active matter: Pattern formation and enhanced flocking. *Phys. Rev. Lett.* **119**, 058002 (2017).

[19] Lenz, P., Joanny, J.-F., Jülicher, F. & Prost, J. Membranes with rotating motors. *Phys. Rev. Lett.* **91**, 108104 (2003).

[20] Kaupp, U. B. & Alvarez, L. Sperm as microswimmers–navigation and sensing at the physical limit. *Eur. Phys. J. Spec. Top.* **225**, 2119–2139 (2016).

[21] Friedrich, B. M. & Jülicher, F. Chemotaxis of sperm cells. *Proc. Natl. Acad. Sci. U.S.A.* **104**, 13256–13261 (2007).

[22] Utada, A. S. *et al.* Vibrio cholerae use pili and flagella synergistically to effect motility switching and conditional surface attachment. *Nat. Commun.* **5**, 4913 (2014).

[23] Di Leonardo, R., Dell'Arciprete, D., Angelani, L. & Iebba, V. Swimming with an image. *Phys. Rev. Lett.* **106**, 038101 (2011).

[24] Zhang, B., Sokolov, A. & Snezhko, A. Reconfigurable emergent patterns in active chiral fluids. *Nat. Commun.* **11**, 4401 (2020).

[25] Kümmel, F. *et al.* Circular motion of asymmetric self-propelling particles. *Phys. Rev. Lett.* **110**, 198302 (2013).

[26] Tsai, J.-C., Ye, F., Rodriguez, J., Gollub, J. P. & Lubensky, T. C. A chiral granular gas. *Phys. Rev. Lett.* **94**, 214301 (2005).

[27] Barois, T., Boudet, J.-F., Lintuvuori, J. S. & Kellay, H. Sorting and extraction of self-propelled chiral particles by polarized wall currents. *Phys. Rev. Lett.* **125**, 238003 (2020).

[28] Liu, P. *et al.* Oscillating collective motion of active rotors in confinement. *Proc. Natl. Acad. Sci. U.S.A.* **117**, 11901–11907 (2020).

[29] Yang, Q. *et al.* Topologically protected transport of cargo in a chiral active fluid aided by odd-viscosity-enhanced depletion interactions. *Phys. Rev. Lett.* **126**, 198001 (2021).

[30] Yang, X., Ren, C., Cheng, K. & Zhang, H. Robust boundary flow in chiral active fluid. *Phys. Rev. E* **101**, 022603 (2020).

[31] Dauchot, O. & Démery, V. Dynamics of a self-propelled particle in a harmonic trap. *Phys. Rev. Lett.* **122**, 068002 (2019).

[32] Li, H. & Zhang, H. Asymmetric gear rectifies random robot motion. *Europhys. Lett.* **102**, 50007 (2013).

[33] Mecke, J., Nketsiah, J. O., Li, R. & Gao, Y. Emergent phenomena in chiral active matter. *Natl. Sci. Open* **3**, 20230086 (2024).

[34] Vega Reyes, F., López-Castaño, M. A. & Rodríguez-Rivas, Á. Diffusive regimes in a two-dimensional chiral fluid. *Commun. Phys.* **5**, 256 (2022).

[35] Caprini, L., Abdoli, I., Marconi, U. M. B. & Löwen, H. Spontaneous self-wrapping in chiral active polymers. *Newton* **1**, 100253 (2025).

[36] Sevilla, F. J. Diffusion of active chiral particles. *Phys. Rev. E* **94**, 062120 (2016).

[37] Qin, S., Budd, R., Bondarenko, S., Liu, W. & Gan, J. Enantioselective degradation and chiral stability of pyrethroids in soil and sediment. *J. Agric. Food Chem.* **54**, 5040–5045 (2006).

[38] Sun, X., Li, G., Yin, Y., Zhang, Y. & Li, H. Carbon quantum dot-based fluorescent vesicles and chiral hydrogels with biosurfactant and biocompatible small molecule. *Soft Matter* **14**, 6983–6993 (2018).

[39] Duan, P., Cao, H., Zhang, L. & Liu, M. Gelation induced supramolecular chirality: chirality transfer, amplification and application. *Soft Matter* **10**, 5428–5448 (2014).

[40] Zhang, J., Chen, Z., Kankala, R. K., Wang, S.-B. & Chen, A.-Z. Self-propelling micro-/nano-motors: Mechanisms, applications, and challenges in drug delivery. *Int. J. Pharm.* **596**, 120275 (2021).

[41] Erkoc, P. *et al.* Mobile microrobots for active therapeutic delivery. *Adv. Ther.* **2**, 1800064 (2019).

[42] Siebers, F., Jayaram, A., Blümler, P. & Speck, T. Exploiting compositional disorder in collectives of light-driven circle walkers. *Sci. Adv.* **9**, eadf5443 (2023).

[43] Ai, B., He, Y. & Zhong, W. Chirality separation of mixed chiral microswimmers in a periodic channel. *Soft Matter* **11**, 3852–3859 (2015).

[44] Meng, F., Liu, J. & He, Y. Transport of the obstacle arrays driven by chiral active particles with temperature difference. *J. Phys. A Math. Theor.* **53**, 095005 (2020).

[45] Lee, J. G., Brooks, A. M., Shelton, W. A., Bishop, K. J. & Bharti, B. Directed propulsion of spherical particles along three dimensional helical trajectories. *Nat. Commun.* **10**, 2575 (2019).

[46] Mijalkov, M. & Volpe, G. Sorting of chiral microswimmers. *Soft Matter* **9**, 6376–6381 (2013).

[47] Li, W., Li, L., Shi, Q., Yang, M. & Zheng, N. Chiral separation of rotating robots through obstacle arrays. *Powder Technol.* **407**, 117671 (2022).

[48] Caprini, L. & Marconi, U. M. B. Active chiral particles under confinement: Surface currents and bulk accumulation phenomena. *Soft Matter* **15**, 2627–2637 (2019).

[49] Caprini, L., Löwen, H. & Marconi, U. M. B. Chiral active matter in external potentials. *Soft Matter* **19**, 6234–6246 (2023).

[50] Joshi, J. & Mishra, S. Analytical theory of chiral active particle transport in a fluctuating density field. *arXiv preprint arXiv:2508.15366* (2025).

[51] Chepizhko, O. & Franosch, T. Ideal circle microswimmers in crowded media. *Soft Matter* **15**, 452–461 (2019).

[52] Makarchuk, S., Braz, V. C., Araújo, N. A., Ciric, L. & Volpe, G. Enhanced propagation of motile bacteria on surfaces due to forward scattering. *Nat. Commun.* **10**, 4110 (2019).

[53] Zöttl, A. & Yeomans, J. M. Enhanced bacterial swimming speeds in macromolecular polymer solutions. *Nat. Phys.* **15**, 554–558 (2019).

[54] Sinaasappel, R. *et al.* Locomotion of active polymerlike worms in porous media. *Phys. Rev. Lett.* **134**, 128303 (2025).

[55] Chepizhko, O. & Peruani, F. Diffusion, subdiffusion, and trapping of active particles in heterogeneous media. *Phys. Rev. Lett.* **111**, 160604 (2013).

[56] Dehkharghani, A., Waisbord, N. & Guasto, J. S. Self-transport of swimming bacteria is impaired by porous microstructure. *Commun. Phys.* **6**, 18 (2023).

[57] Morin, A., Desreumaux, N., Caussin, J.-B. & Bartolo, D. Distortion and destruction of colloidal flocks in disordered environments. *Nat. Phys.* **13**, 63–67 (2017).

[58] Li, M., Zheng, N. & Li, Y. Migration of an active particle in mixtures of rigid and flexible rings. *Phys. Rev. E* **111**, 035412 (2025).

[59] Leoni, M. & Liverpool, T. Dynamics and interactions of active rotors. *Europhys. Lett.* **92**, 64004 (2010).

[60] Mandal, R., Bhuyan, P. J., Chaudhuri, P., Dasgupta, C. & Rao, M. Extreme active matter at high densities. *Nat. Commun.* **11**, 2581 (2020).

[61] Li, Y.-W. *et al.* Long-wavelength fluctuations and anomalous dynamics in 2-dimensional liquids. *Proc. Natl. Acad. Sci. U.S.A.* **116**, 22977–22982 (2019).

[62] Ebbens, S., Jones, R. A. L., Ryan, A. J., Golestanian, R. & Howse, J. R. Self-assembled autonomous runners and tumblers. *Phys. Rev. E* **82**, 015304 (2010).

[63] Van Teeffelen, S. & Löwen, H. Dynamics of a brownian circle swimmer. *Phys. Rev. E* **78**, 020101 (2008).

[64] Wykes, M. S. D. *et al.* Dynamic self-assembly of microscale rotors and swimmers. *Soft Matter* **12**, 4584–4589 (2016).

[65] Duncan, P. D. & Camp, P. J. Structure and dynamics in a monolayer of dipolar spheres. *J. Chem. Phys.* **121**, 11322–11331 (2004).

[66] Kumar, N., Soni, H., Ramaswamy, S. & Sood, A. Flocking at a distance in active granular matter. *Nat. Commun.* **5**, 4688 (2014).

ACKNOWLEDGEMENTS

We acknowledge the supports of the National Natural Science Foundation of China (Grants No. 12374205, No. 12304245, No. T2325027, No. 12274448, and No. 12475031), the Shandong Provincial Natural Science Foundation (Grant No. ZR2024YQ017), the Science Foundation of China University of Petroleum, Beijing (Grants No. 2462024BJRC010 and No. 2462023YJRC031), and the Beijing Institute of Technology Research Fund Program for Young Scholars. This work was also supported by Beijing National Laboratory for Condensed Matter Physics (Grants No. 2024BNLCMPKF009).

AUTHOR CONTRIBUTIONS

N.Z., L.N., P.L. and M.Y. conceived the research. N.Z., L.N. and K.Z. conducted the experiments. K.Z., Y.T., H.Z. and X.Y developed the video analysis code. K.Z. and H.Z. performed data analysis. N.Z., L.N., P.L., M.Y. and Y.L. supervised the research. All authors discussed the results and contributed to writing the manuscript.

COMPETING INTERESTS

The authors declare no competing interests.

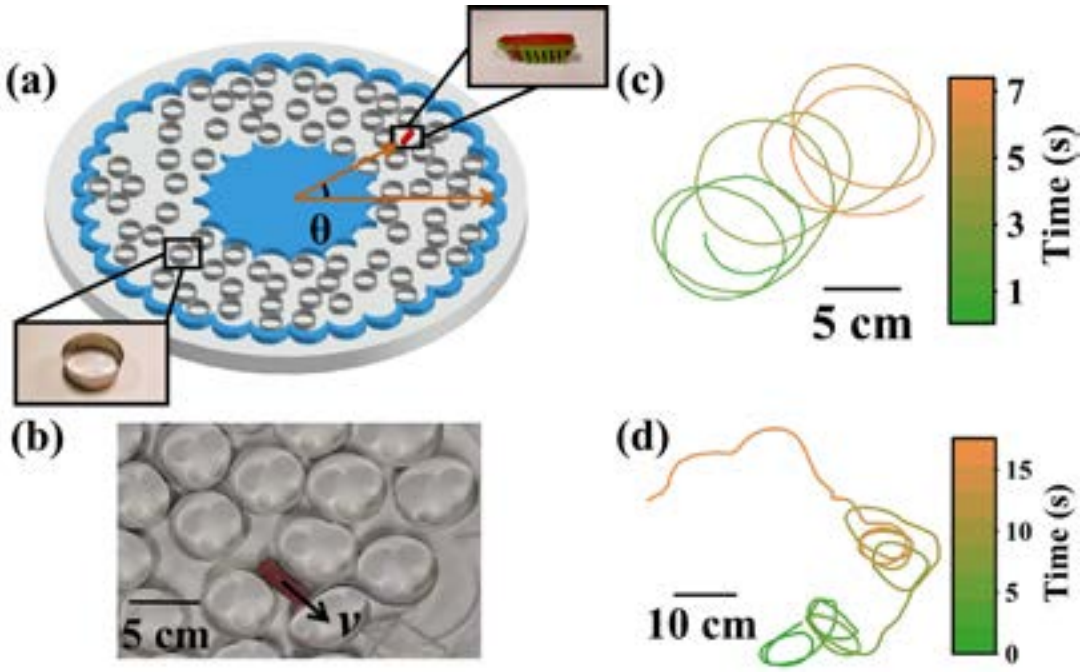
(a)
θ
(b)
5 cm
v
(c)
5 cm
7
5
3
1
Time (s)
(d)
10 cm
15
10
5
0
Time (s)

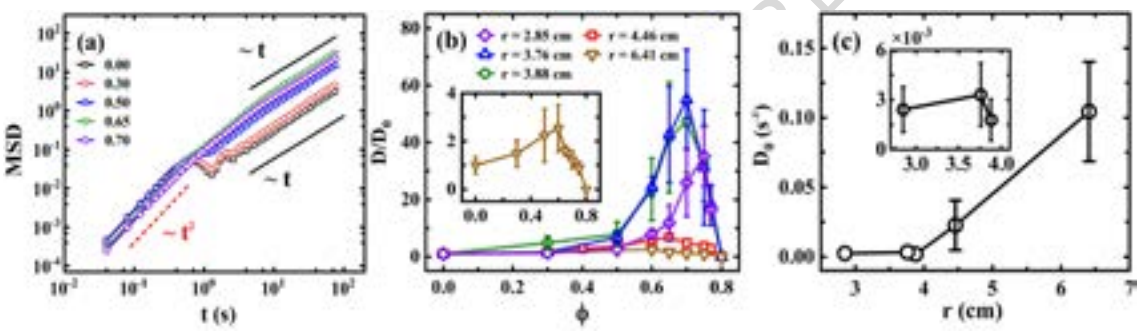

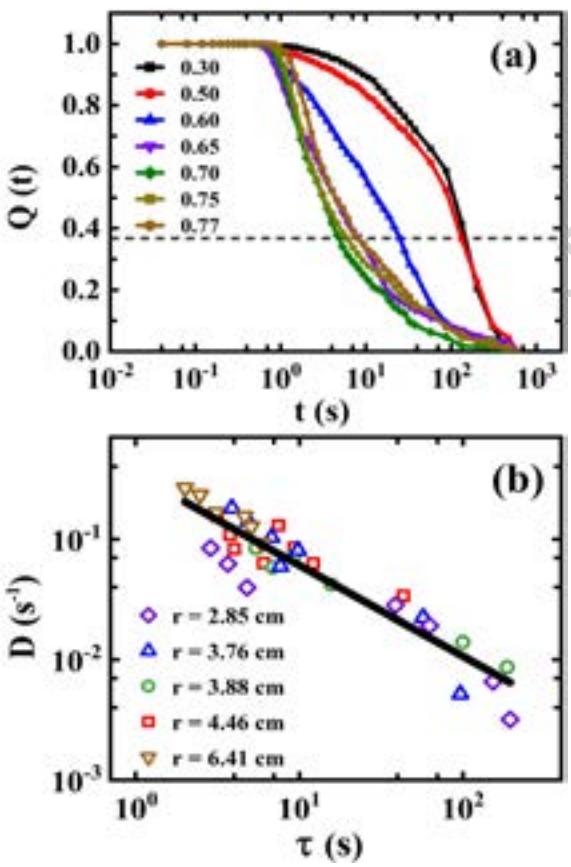
(a)
Q (t)
t (s)
0.30
0.50
0.60
0.65
0.70
0.75
0.77
(b)
D (s^{-1})
τ (s)
r = 2.85 cm
r = 3.76 cm
r = 3.88 cm
r = 4.46 cm
r = 6.41 cm

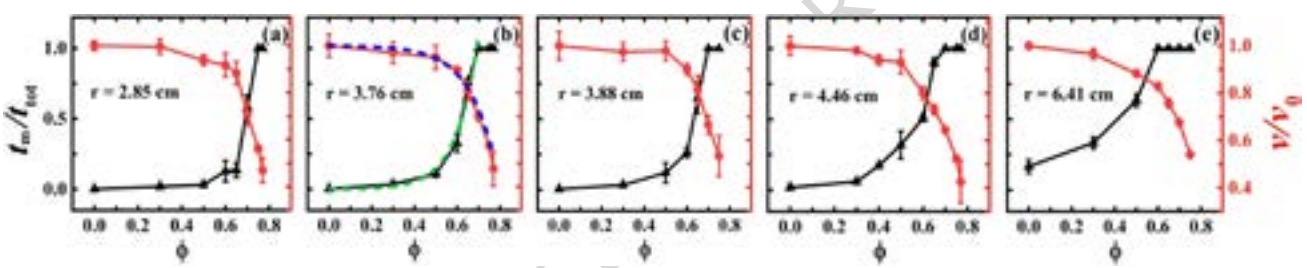

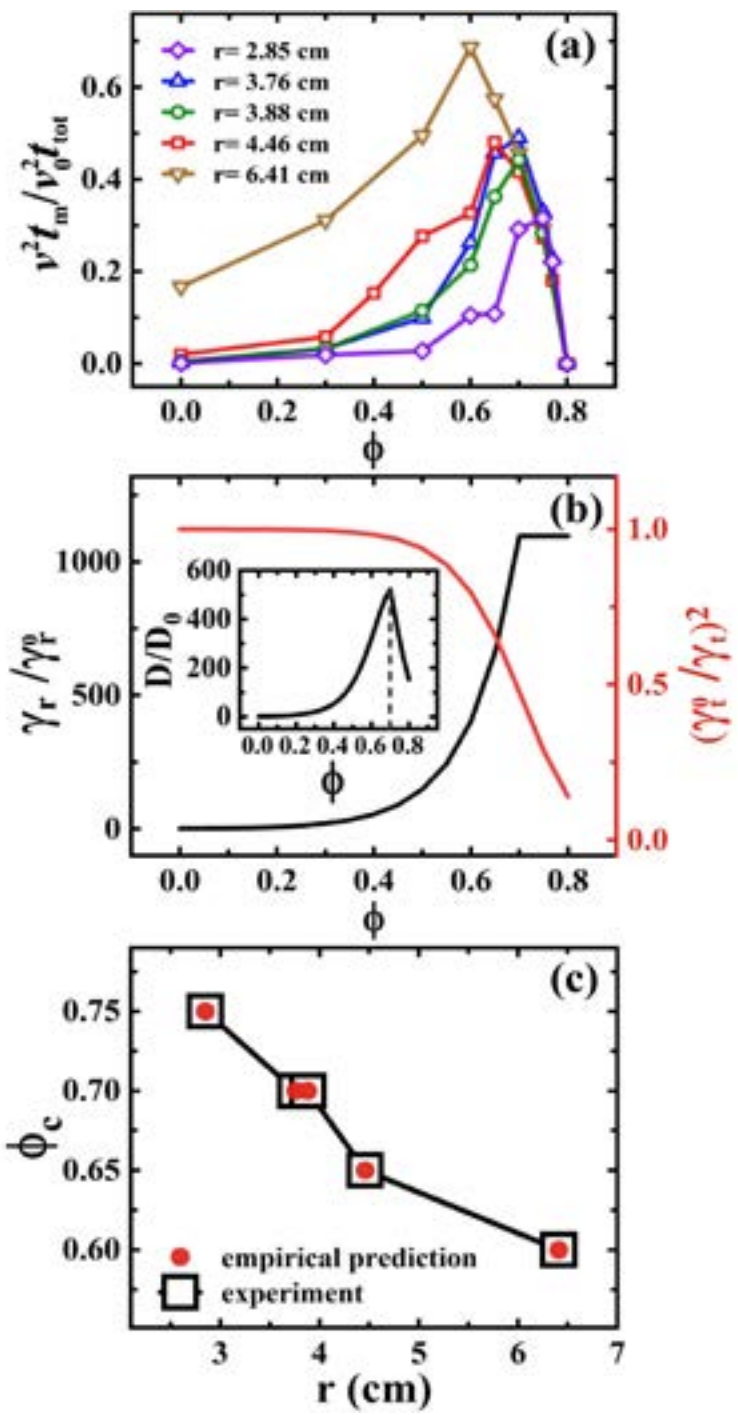
(a)
r= 2.85 cm
r= 3.76 cm
r= 3.88 cm
r= 4.46 cm
r= 6.41 cm
$v^2 f_m / v_0^2 f_{tot}$
0.0
0.2
0.4
0.6
0.0
0.2
0.4
0.6
0.8
ϕ
(b)
γ_r / γ_r^0
1000
500
0
D/D$_0$
600
400
200
0
0.0 0.2 0.4 0.6 0.8
ϕ
$(\gamma_t^0 / \gamma_t)^2$
1.0
0.5
0.0
0.0
0.2
0.4
0.6
0.8
ϕ
(c)
ϕ_c
0.75
0.70
0.65
0.60
empirical prediction
experiment
3
4
5
6
7
r (cm)

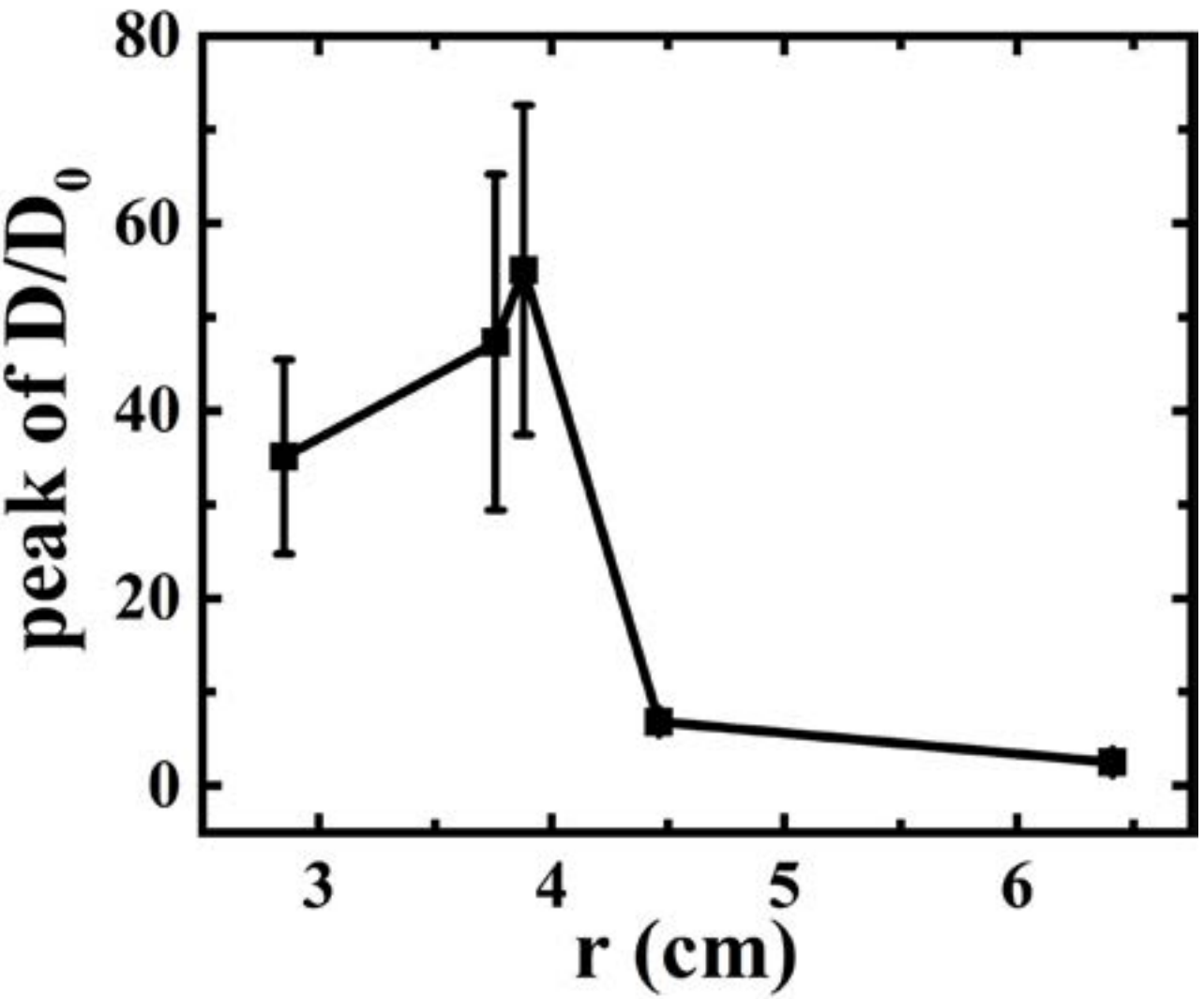
80
60
40
20
0
peak of D/D0
3
4
5
6
r (cm)

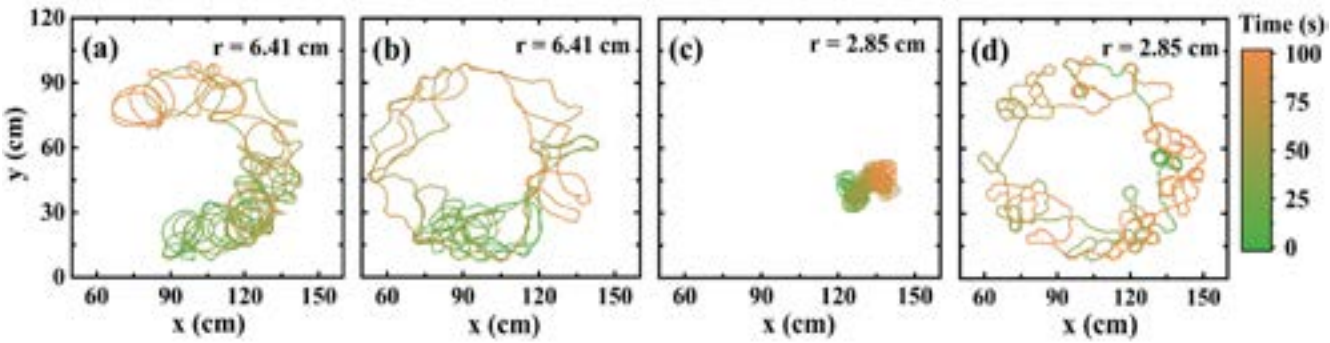

Robot	1	2	3	4	5
r (cm)	2.85	3.76	3.88	4.46	6.41
v_0 (cm/s)	24.04 ± 0.94	23.39 ± 1.11	22.28 ± 0.70	26.12 ± 0.61	24.95 ± 0.75
ω_0 (s^{-1})	8.43 ± 0.24	6.23 ± 0.21	5.73 ± 0.13	5.85 ± 0.21	3.89 ± 0.28
T (s)	0.74	1.01	1.10	1.07	1.61
Dr (s^{-1})	0.39 ± 0.095	0.24 ± 0.053	0.14 ± 0.023	0.24 ± 0.064	0.27 ± 0.071
τ_r (s)	2.56	4.17	7.14	4.17	3.70
l (cm)	61.44 ± 2.4	97.54 ± 4.6	40.91 ± 5.0	108.9 ± 2.5	92.32 ± 2.8